Supplementary information of the manuscript

Picoliter nDEP traps enable time-resolved contactless single bacterium analysis in controlled microenvironments

Frederik S. O. Fritzsch[a], Katrin Rosenthal[a], Anna Kampert[a], Steffen Howitz[b], Christian Dusny[a], Lars M. Blank [a#], and Andreas Schmid [a*]

[a] *Laboratory of Chemical Biotechnology, TU Dortmund University, Emil-Figge-Str. 66, D-44227 Dortmund, Germany, E-mail: andreas.schmid@bci.tu-dortmund.de, Fax: +49 231 755 7382; Tel: +49 231 755 7380*

[b] *GeSiM Gesellschaft fuer Silizium-Mikrosysteme mbH, Bautzner Landstrasse 45, D- 01454 Grosserkmannsdorf, Germany*

 # Present address: iAMB - Institute of Applied Microbiology, ABBt – Aachen Biology and Biotechnology, Worringerweg 1, D-52074 Aachen

*Corresponding author: Andreas Schmid

Table of supplementary material

Principal basics of DEP cell manipulation

Pohl defined DEP as the motion of particles relative to that of the solvent, resulting from polarization forces produced by an inhomogeneous electric field.[1] In an electrical field a particle is polarized and can be simplified described as a dipole. In a high frequency alternating electrical fields, orientation of these poles a not aligned as fast as the field vectors change. The difference in orientation leads to the dielectrically force. Jones described the resulting dielectrical force as shown in equation 1.[2]

$$\vec{F}(t) = (\vec{m}(t) \cdot \nabla)\vec{E}(t) \quad (1)$$

While the inhomogeneous electrical field $\vec{E}(t)$ can be adapted by the geometry of electrodes and generator control, the effective dipole moment $\vec{m}(t)$ is also influenced by the properties of particles and the dielectricum, which Jones summarized for a spherical particle with equation 2.

$$\vec{m}_{eff}(t) = 4\pi R^3 \varepsilon_m \mathrm{Re}(CM)\vec{E}(t) \quad (2)$$

The equation considers the interplay of an electrostatic potential of a point shaped dipole and the potential of the dipole surrounding medium in an inhomogeneous electrical field.[3] Cells exhibit a conductivity associated with mobile ions in there structures which is considered in the Clausius-Mossotti factor f_{CM}. The factor is a function of the complex permittivity of the cell $\tilde{\varepsilon}_c$ and the medium $\tilde{\varepsilon}_m$, which in term can be described as a function of the electrical constant in vaccum ε_0, the applied frequency ω of an inhomogeneous electrical field and the dielectric constants ε and electrical conductivity σ_C of the cell and σ_m of the medium (Equation 3).

$$CM = \frac{\tilde{\varepsilon}_c - \tilde{\varepsilon}_m}{\tilde{\varepsilon}_c + 2} = \frac{\sigma_c + i\omega\varepsilon_0\varepsilon_c - \sigma_m + i\omega\varepsilon_0\varepsilon_m}{\sigma_c + i\omega\varepsilon_0\varepsilon_c + 2\sigma_m + 2i\omega\varepsilon_0\varepsilon_m} \quad (3)$$

Depending on the medium and cell properties the Clausius-Mossotti factor f_{CM} can become positive for example in case of $\sigma_c > \sigma_m$ or negative in case of $\sigma_c < \sigma_m$ which is referred to positive dielectrophoresis or negative dielectrophoresis. While positive dielectrophoresis leads to the attraction of the particles to electrical field maxima, negative dielectrophoresis leads to the attraction of the particles to electrical field minimum. The field maxima or highest fields intensities can be found at the interface of the electrodes to the medium, which explains the attraction of cells to the electrodes in case of pDEP and the repellency in case of nDEP when manipulating cells or particles in a microfluidic stream (Fig. 1).

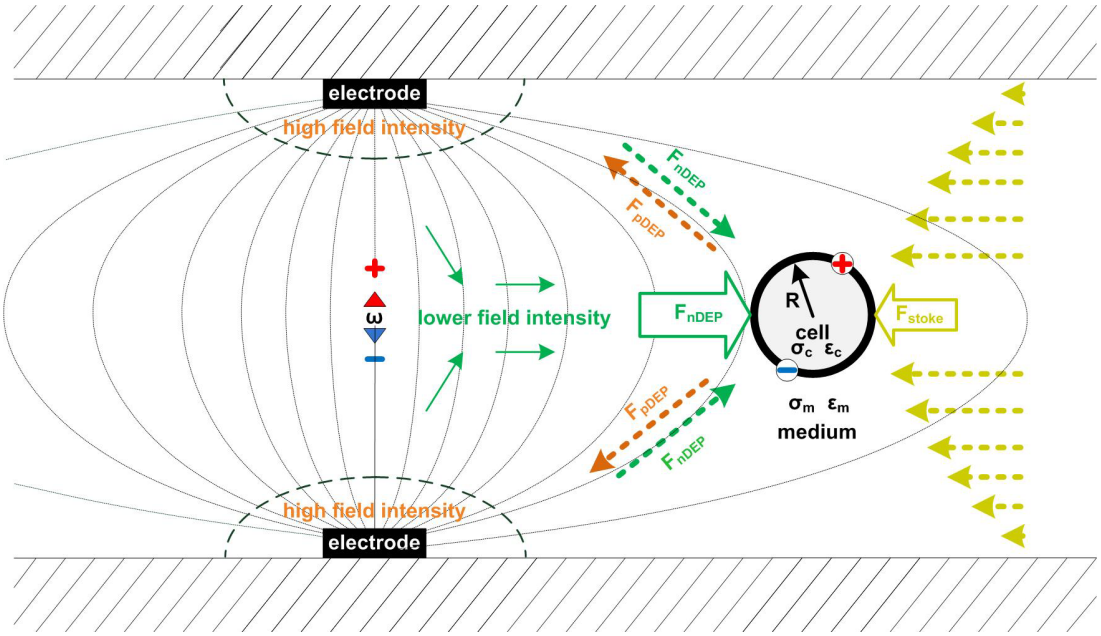

Figure 1: Schematic drawing of basic impact factors based on fundamental theory for DEP cell manipulation in a microfluidic stream.

Next to the conductivity, the applied frequency ω and the dielectric constants influence the polarization of the cell and lead to a change of sign of the Clausius-Mossotti factor f_{CM}. With the dipole approximation of Jones the DEP force can be averaged over time (rms = rot means square) and summarized to equation 4.

$$\vec{F}_{DEP} = 2\pi\varepsilon_m R^3 \mathrm{Re}(f_{CM}) \nabla E^2{}_{rms} \quad (4)$$

In the most multielectrode configurations equation 4 describes the resulting dielectrical force sufficiently.[4] However, the assumption of a spherical cell does not consider different cell morphologies, which were partly considered by Morgan and Green for rod shaped bacteria.[5, 6] The approximation also does not consider the inhomogeneous dielectric properties of dynamic changing cells with their thousands of vesicles. The heterogeneous intracellular structures were first considered by the multi-shell model,[7] which was later extended for non-spherical cell [8] and by considering the dielectric anisotropy of the plasma membrane.[9]

Impact microelectrode geometry on nDEP cell manipulation

Independent from frequency or dielectric constants, the DEP force can be changed by increasing applied voltages or lowering the electrode distance. The electrode geometry has a significant impact $\nabla(E_{rms})^2$ in equation 4, which has the dimension of U^2m^{-3}.[10] Schnelle *et al.* demonstrated the significant impact of electrode distance between semi-infinite plate electrodes on nDEP approximated with

$$F_{DEP} = \frac{27}{32}\pi^2\,\varepsilon_m\,R^3 CM\,\frac{U_{rms}^2}{d^3} \quad (5)$$

in which d is the distance of electrodes.[11] In this work the electrode tip distance of octupoles where reduced maintaining a symmetrical cube between the electrode tips. The description of nDEP forces on a cell in non-uniform electrical field can be refined by incorporating with multipole theory, which can be deducted from an important theorem of electrostatics published by Stratton in 1941.[12] Derived from this theorem, the potential of the DEP force in multipoles can be calculated as the sum over the multiforce contributions with

$$F_{DEP} = U_{rms}^2 \sum_{n=1}^{\infty} \left(\vec{\alpha}_n \left(\frac{\vec{x}}{g}\right) \left(\frac{R}{g}\right)^{2n+1} Re[CM[\omega]] \right) \quad (6)$$

considering a point charge with n=0, a dipole with n=1, a quadrupole with n=2 and an octupole with n=3 (and so on). The geometric properties of the electrode configuration is presented by the vector functions α_n, which can rarely be expressed for 3-D electrode configurations.[13] With the coordinate x and the dimension of electrode system g, a finite difference method must be used to solve equation 6.[4] However, to calculate a realistic nDEP force on a cell previous mentioned models for inhomogeneous properties of cells and medium have to considered in multipole induced inhomogeneous field distributions which is not in the scope of this work.

nDEP used for single cell manipulation in microfluidic streams

For the manipulation of cells in microfluidic streams the DEP force has to exceed the flow resistance, which is labeled in Figure 1 as F_{Stoke}.

$$F_{DEP} > F_{Stoke} = 6\pi\eta\nu R \quad (7)$$

pDEP manipulation is often more stable in microfluidics because it leads to the trapping of cells on the electrode surface, where cells experience significant lower fluidic velocities compared to cells which are nDEP manipulated to the field intensity minimum between the electrode where the parabolic microfluidic flow profiles find their velocity maximum (indicated in figure 1). Additionally, pDEP trapping is supported by direct contact forces of the electrodes, while cells manipulated with nDEP are floating and moving. Despite the bigger challenge to manipulate cells by contactless nDEP forces, this technology is less influence a living organisms owing to cell trapping in electrical field intensity minimum and the exclusion of interactions with solid surface and its chemistry.

The effective contactless single bacterium manipulation via nDEP forces in this work, required to optimize three-dimensional arrangements of microelectrode geometries in microfluidic profile designs. The aimed balancing of nDEP and Stokes forces in optimized geometries led to configurations which required less nDEP forces for effective cell manipulation. For example the cell deflection by linear dipoles in microfluidic flows was optimized by setting a different angles of linear dipole electrodes in xy orientation to the xy orientation stokes force (Fig. 2).

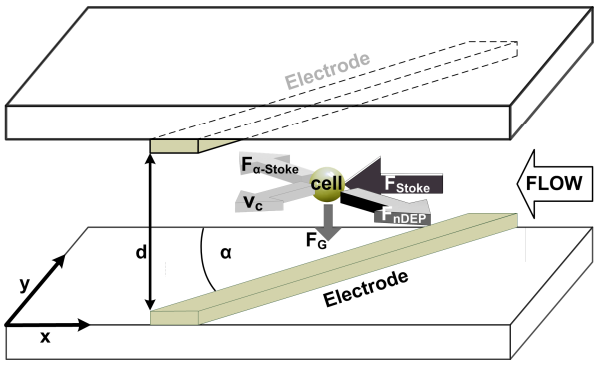

Figure 2: Forces during cell deflection by nDEP in a microfluidic stream.

α in figure 2 describes the angel between the flow direction and linear dipoles. Decreasing the α results in lower nDEP forces required to overcome F_α-Stoke and hence to deflect a cell in the direction v_C along the electrodes (Fig. 2). The required nDEP forces F_{nDEP} can be described by equation 8.

$$F_{DEP} > F_{\alpha-Stoke} = 6\pi\eta v R \sin\alpha \quad (8)$$

Integration of equation 8 in equation 5 allows the approximation of maximal microfluidic velocities in equation 9 which can be applied for cell deflection with semi-infinite dipole electrodes, dependent on electrode distance and flow direction.

$$v_{max} = \frac{9}{64\eta}\pi\varepsilon_m R^2 CM \frac{U_{rms}^2}{d^3 \sin\alpha} \quad (9)$$

In this work fluidcs and electrodes were optimized to manipulate small bacteria by nDEP instead of simply rising the voltages because higher voltage accompany with increasing Joule heating which finally results in not live sustaining microenvironments.[14, 15]

nDEP for microenvironmental controlled single cell analysis

Noninvasive cell manipulation avoids exceeding cell damaging temperatures, which leads to a significant limitation of maximal applicable voltages for nDEP force. To a certain extent, Joule heating is reducible by lowing electrode distance owing to a reduction of dielectric volume influenced by the electrical field between the electrodes. Additionally the thermal heat transfer with higher surface to volume ratios is higher in further miniaturized channels. The heat transfer can be futher optimized by selection of materials with high thermal conductivities. However, the reduction of electrode distance is limited to the dimension of cells and to current available DEP chip micromanufacturing technologies. Rapid developments in micromanufacturing technologies and optimization of microelectrode geometries in the last decades, nDEP became applicable for sorting and trapping of single cells in stream of media. The first single cell nDEP trapping in three dimensional high frequency alternating electrical field minima was accomplished in 1992 with 10 - 20 µm sized cells by Schnelle *et al.* [16] In their work the scientists introduced octupole electrode configurations for contactless single cell trapping and precisely described several possible nDEP field controls and their impact on particles and cell deflection. [11, 16-28] In not streaming microfluidic volumes the technology was even used to accumulate small virus particles. [19, 29, 30] However, only in 2008 the optimization of octupole geometries and fluidic control allowed the nDEP trapping of a single cell in a microfluidic streams to supply it with a defined nutrients and oxygen supply. [28, 31] The constant contactless perfusion of a single cell in a gentle laminar microfluidic flow allowed a continuous removal of extracellular metabolites and hence a constant microenvironment. To ensure a defined chemical environment biocompatible and chemical inert surface are important owing to intensive interaction of channel material boundaries with the medium microfluidic chips with high surface to volume ratios. Non biocompatible materials can influence the cellular physiology and might influence results of single cell analysis. Living cells respond to microenvironments with a change in their cellular physiology, which can even change their conductivity and dielectric properties.[32] Especially the changing composition of their cell wall and membrane has significant impact on resulting DEP force.[33] To sum up, an nDEP chips designer has to consider interplaying properties of the chip, the medium and the cell (Fig. 3).

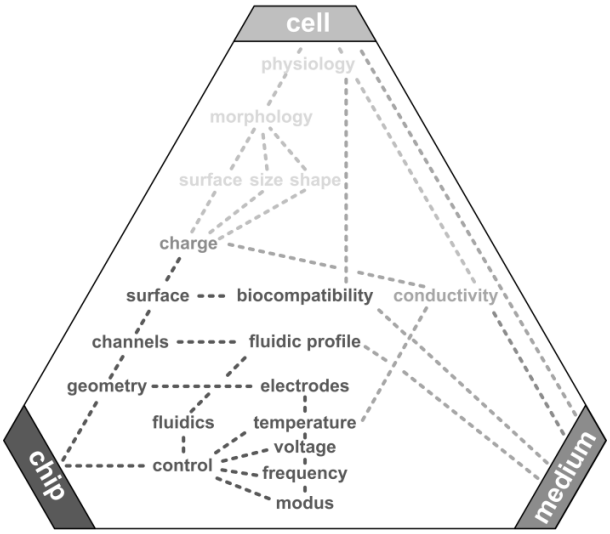

Figure 3: Examples of main nDEP force influencing and interplaying properties of the chip, medium and manipulated cell. The consequent consideration of the introduced and in figure 5 summarized nDEP principals and interplaying properties of the chip, medium and targeted cells was used in this work to develop the Envirostat 2.0.

Microfluidic and microelectronic setup of the Envirostat 2.0

The used fluidic and electrical interface was described in detail before[34] and was adapted to the Envirostat 2.0 chip design in terms of electrical and fluidic connections (Fig. 4 and Fig. 5). A constant medium flow condition in the Envirostat 2.0 channels was achieved by using SP210IWZ syringe pumps (World Precision Instruments Inc., USA) equipped with 10 - 250 µL glass syringes (ILS Innovative Labor Systeme GmbH, Germany). The generator for microelectrode control (Cytocon 400, PerkinElmer, USA) and the pumps were remote controlled by the software Switch (PerkinElmer, USA). Images and videos were taken by a CCD-camera (EHDkamPro02, EHD Imaging, Germany) connected via a video coupler (DC 50 W) to an inverted microscope (IX71 Olympus, Japan) with appropriate filters and objectives. Pictures from the CCD-camera were acquired by a video grabber card (Impact-VCB, Hauppauge, Germany), displayed and stored via the software WinTV (Hauppauge Computer Works GmbH, Germany). Before the Envirostat 2.0 can be applied for the isolation and trapping of a microbe, it has to be integrated in the Envirostat 2.0 periphery shown in figure 4. The periphery allows a PID regulated external temperature control by Peltier elements above the chip for heating and cooling and the shown temperature sensor placed under the chip for temperature sensing (Fig. 4).

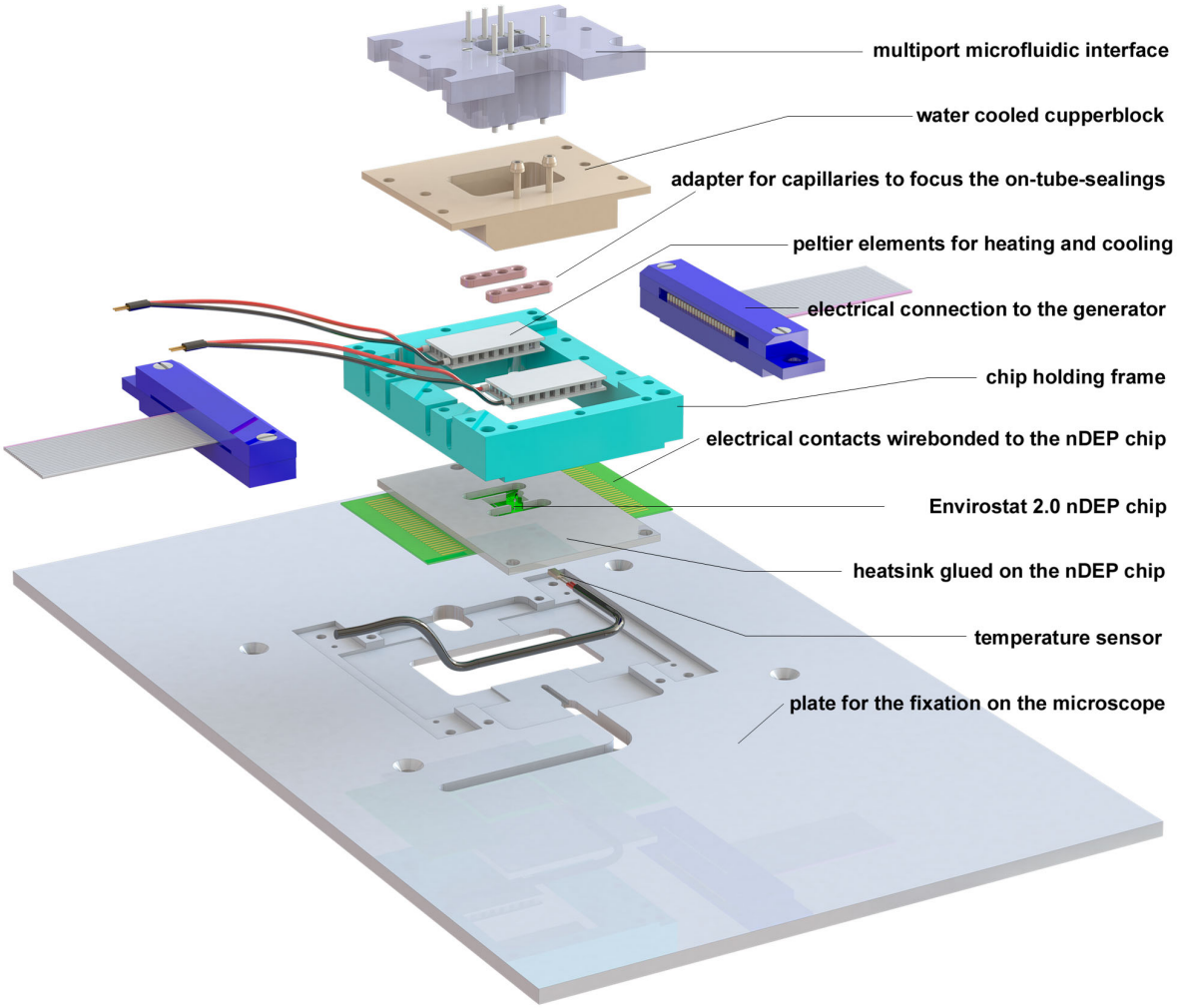

Figure 4: The Envirostat 2.0 interface

For sampling of single bacterium perfusion medium from outlet 5 (Fig. 1 in the manuscript) the adapter shown in figure 4 precisely centering an on-tube-seal integrated in used capillaries on the outlet. The on-tube-seal was described before and allows a minimal dead volume during sampling.[35] The Envirostat 2.0 chip comprised a novel microelectronic structure which integrates sorting and trapping elements. Hence a new microelectronic and -fluidic control required the programming of a new software interface to control the generator and fluidic pumps using the program Switch (PerkinElmer, USA). To program a generator control with different functions each implemented electrode has to be connected to the generator plugins. The microelectronic connections and setup applied in this work are illustrated in figure 5.

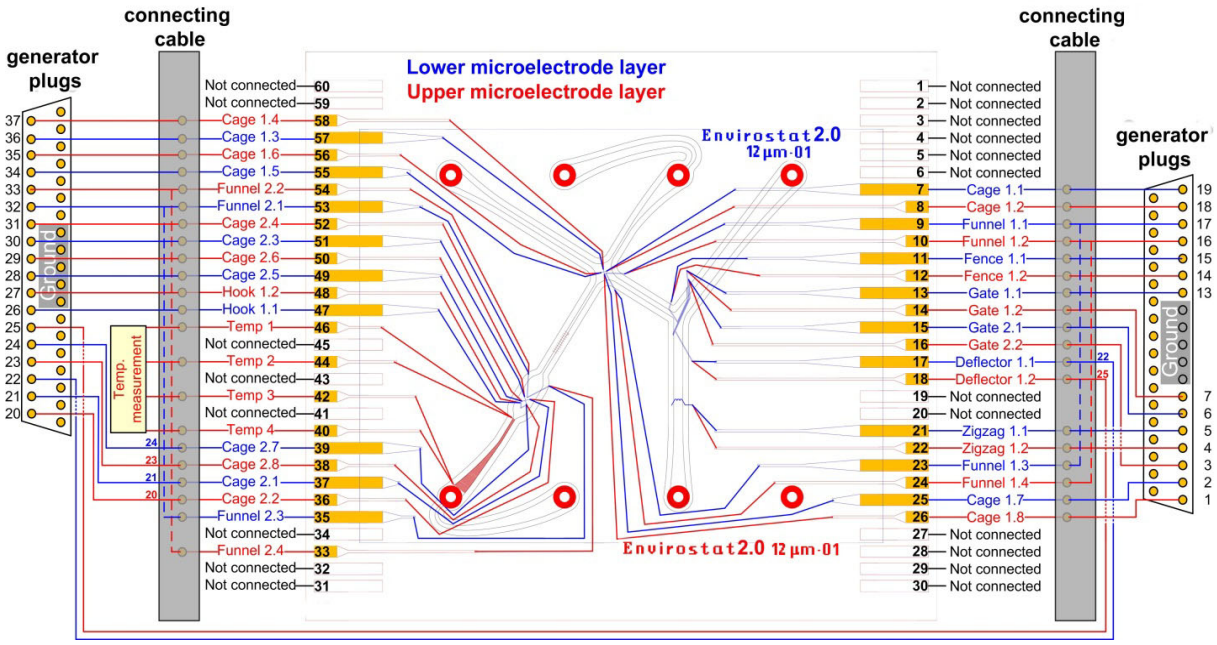

Figure 5: Microelectronic setup of the Envirostat 2.0

The on-chip-temperature measurement sensor shown in figure 5 (Temp. measurement) can be used as a more sensitive alternative to the external sensor illustrated in figure 4 and was applied to test the temperature control by the modified and adapted Envirostat 2.0 interface.

Microfluidic control calibrations

To ensure that fluidic velocities around an isolated and contactless cultivated single bacterium are defined the adjusted volumetric flows by microfluidic syringe pumps (World Precision Instruments Inc., USA) equipped with 10 - 250 µL glass syringes (ILS Innovative Labor Systeme GmbH, Germany) used for this work were precisely calibrated using fused silica capillary with highly defined inner diameter of 30 µm (Fig. 6).

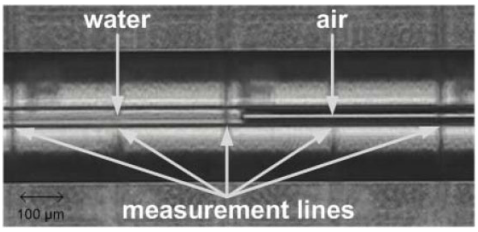

Figure 6: Fused silica on lithographic structured foil.

By gluing the fused silica on a foil with lithographic structured scaling of 100 µm squares enabled precisely volumetric measurement connecting the capillary behind a lab-on-a-chip system (Fig. 7).

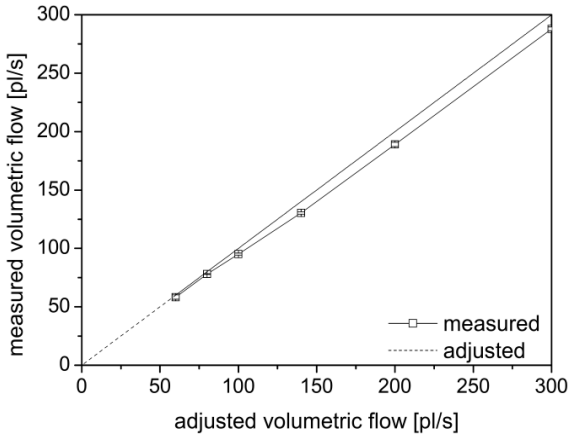

Figure 7: Control of volumetric flow

The single cell cultivations were performed applying an adjusted volumetric flow of 80 pL s^{-1} (4.8 nL min^{-1}) which was precisely adjustable applying the described pumps with 10 µl syringes. Calculated from the fluidic simulations (Fig. 2 in the manuscript), this volume flow resulted in the wanted fluidic stream velocity of 10 µm s^{-1} in the octupole cage center.

Flow simulation control by micro particle imaging velocimetry (µPIV) measurements

All simulations were performed using the program Solidworks Simulation 2010 (Solidworks Corporation, USA). The equations used in the software are based on the Navier-Stokes equations and can be looked up in the technical reference of the program. Owing to Reynolds numbers below 1 resulting from the applied properties of water and volumes flows up to 1 ml h^{-1} in microchannel systems, laminar flows were assumed in all simulations. Table 1 shows initial mesh adjustments used for all simulations.

Tab. 1: Settings of number of cell for initial mesh

number of cells per mm in the	x- axis	y- axis	z- axis
Cytocon chip (PerkinElmer, USA)	50	50	240
Envirostat 2.0 (12 µm design)	50	50	240
Envirostat 2.0 (20 µm design)	35	35	240

The temperature was adjusted to 20°C and the microchannel walls were assumed to be adiabatic. To test if the simulation parameters and assumtions simulated realistic microfluidic velocity fields in similar sized microchannels, we compared simulations of the programm Solidworks with results of micro particle imaging velocimetry (µPIV) measurements, performed under similar conditions as adjusted in the simulation. Hence a commercial available nDEP chip (Cytocon chip, PerkinElmer, USA) with a different chip design but similar microchannel dimensions was used to test the quality of simulation data (Fig. 8). The same set of simulation parameters were later used to develop the new channel design, to position the microelectrodes and for the fluidic characterization of the final Envirostat 2.0 design. The µPIV measurements were performed using fluorescent 2.1 µm sized particles (19814, Polysciences Europe GmbH, Germany) in a volumetric flow of 1 ml h^{-1} (Fig. 8 (C)). The microchannel

structure of the Cytocon chip was imported to Solidworks 2010 (Solidworks Corporation, USA) from an AutoCAD file (.dwg 2000, Autodesk, Inc., USA) which was used for production of the chips. The model had a channel height of 28 µm (manufactured channel height 28 +/- 0.3 µm).

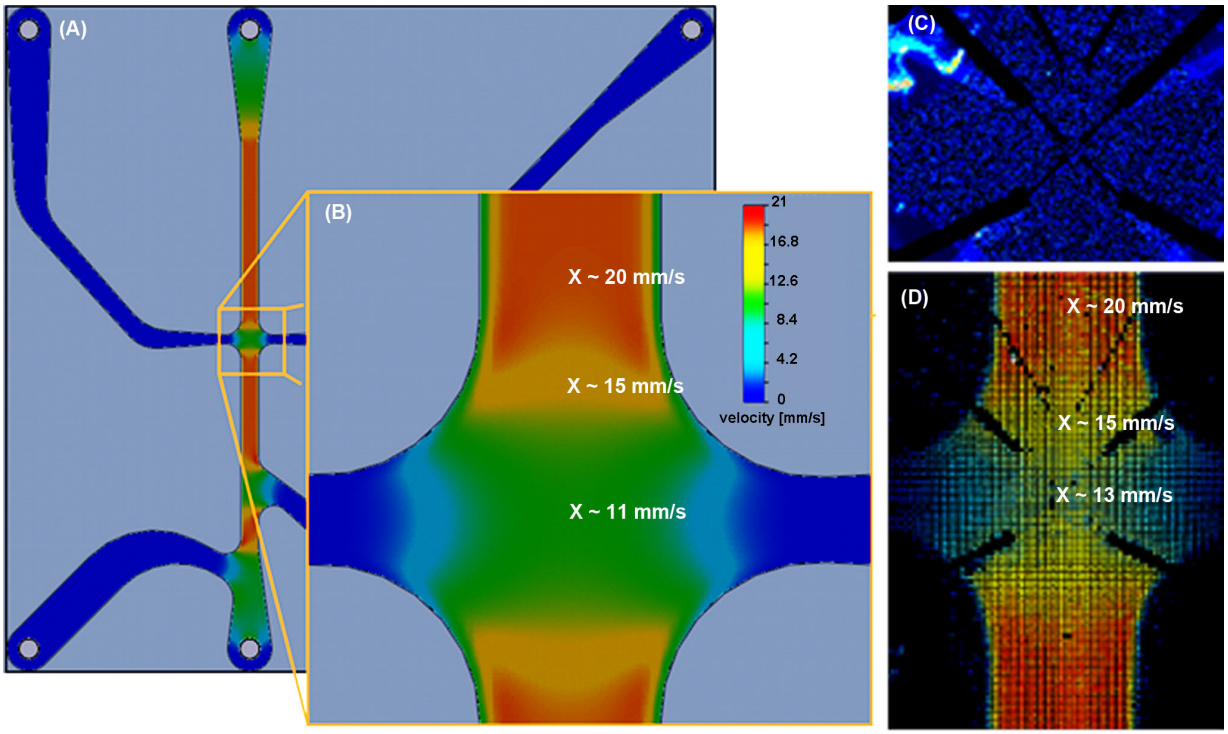

Figure 8: Control of simulation settings by comparison of simulation data to µPIV measurements in a commercial Cytocon chip. (A) Total microchannel structure of the Cytocon chip. (B) Magnification of velocity field in the cross section. (C) Microscopic fluorescent picture of the applied fluorescent particles. (D) Results of velocity field profile in the cross section of the Cytocon chip calculated from the µPIV measurements.

The comparison of the µPIV measurements with the simulation results showed, that the simulation resulted in microfluidic velocity fields which had a good agreement with the µPIV measurements (comparing Fig. 8 (B) and (D)). Hence, the fluidic characterization of fluidic velocity fields and the consequent positioning of microelectrodes presented in the manuscript are precise, which correlates with observed trajectories of cells applying the presented Envirostat 2.0 chip.

Materials and basic methods used for micro manufacturing

The following materials have been used for chip manufacturing: upper and lower glass substrates (borosilicate glass, type D263, Berliner Glas AG, Germany) with microelectrode arrays (10 nm Ti, 100 nmPt) were spun with SU-8-10 or SU-8-20 (Micro Resist Technology GmbH, Germany) using a RC-8 spin coater (SussMicroTec Lithography GmbH, Germany) to retrieve spacer heights of 12 µm and 20 µm, respectively. After a softbake at 90°C for 120 s, a UV-exposure was performed in a MA-25 mask aligner (SussMicroTec Lithography GmbH, Germany) for 25 s at 10 mW cm−2. In the following post exposure bake at 90°C for 90 s, the substrates were developed in XP SU-8 developer and subjected to a final hardbake at 150°C for 300 s using a hotplate (Präzitherm PZ 282, Stoerktronic, Germany). As a result, the SU-8 spacer with the structure shown in figure 3 (B) of the manuscript was created on the 175 µm thick top glass. Before the bonding of top and bottom glass chip, a dotted line of 350 nl SU-8-5 adhesive droplets was dispensed in a non-contact mode along the 12 µm thick SU-8-10 spacer. The SU-8-5 was mixed one to one with SU-8-5/GBL. The wet SU-8-5 mixture works as an UV-curable adhesive. The SU-8-5 dispense process along the channel spacer was performed with the Nano-Plotter TM (GeSiM mbH, Germany) by a drop on demand technology. To follow the reservoir channel for SU-8 depositioning (as indicated in figure 3 (B) of the manuscript) of the Envirostat 2.0 chip, each dispense position has to be computed by the integrated, video microscope based imaging system. The available software interface between the Autocad CAD, software used for spacer design, and the Nano-Plotter software NPC16 guaranties that this process runs reliable and efficiently. After SU8-5 dispensing, the upper and the lower glass substrate of the Envirostat 2.0 chip stack, have to assemble in a so called flip chip packaging process. Therefore, both pre-treated glass chips have to be assembled face to face, after they are aligned precisely. The alignment accuracy of such a chip stack is plus minus 3 µm and was performed with an aligner (also named as fineplacer) (Joerns GmbH, Germany). Next to SU-8 a UV-curable adhesive Vitralit 1558 (Panacol-Elosol GmbH, Germany) was used as supporting glue for the sub 20 µm channel heights (mentioned in figure 3 (C) of the manuscript as liquid glue) and the screen printed SMT adhesive PD955 (Heraeus Holding GmbH, Germany) was used for the standard glue process as described in the manuscript. Next to the here mentioned PD955 adhesive, a large number of other UV curable SMT adhesives can be used, but screen printing adhesives bring in their own minimal height (e.g. PD955PY, PD955PRM, PD955PRH, PD955M, PD205A-Jet; PD208PR, PD208M → >20-25 µm possible (Heraeus Holding GmbH, Germany) or e.g. 3M™ Screen Printable UV-Curing Adhesive 7555, 3M, USA) → >25 µm possible, etc.) and could not be used to manufacture nDEP chips with channel heights < 20 µm. Supplemental to figure 3 of the manuscript, the following figure 9 shows examples of manufactured chips (Fig. 9 (A, a, b)) and a not colored version of the comparison between chip channels bonded with the screen-printed SMT adhesive PD955 and chip channels bonded with the presented Envirostat 2.0 bonding technology using only biocompatible SU-8.

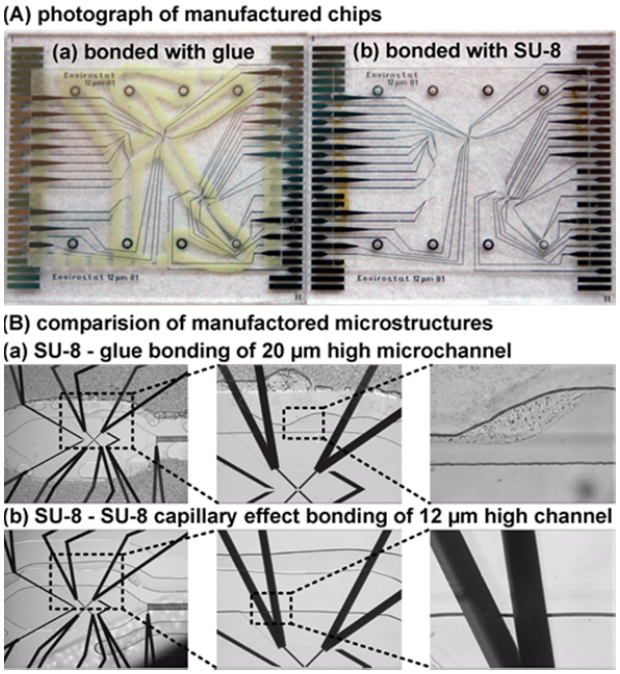

Figure 9: Comparison of bonding technologies. (A) Photograph of a chips without a heat sink. (a) chip bonded with the screen-printed glue. (b) A
245 chip bonded with SU-8. (B) Microscopic view on bonded microchannels (a) Microchannel bonded with the screen-printed glue. (b) Microchannel structures after bonding with the optimized SU-8 capillary-effect-bonding for a biocompatible and defined sealing.

Temperature control of the Envirostat 2.0 interface

The chip interface was modified and used to control the temperature in the Envirostat 2.0 chip (Fig. 4). To test if the modified periphery precisely controls the temperature in the Envirostat 2.0 chip, the regulated temperature was additionally correlated to temperature sensitive resistance, implemented as on-chip temperature sensor. The meander–like formed on-chip sensor was placed behind the second cage, close to the cultivation section of the chip. The resistance of the electrode was measured 10 s after the temperature adjustment by the new chip periphery shown in figure 4. The measurement was performed with a multimeter (VA-18B, KomercioHG, Ebern Germany) applying a 4-point (Kelvin) resistance measurement method.[36] Figure 10 shows a clear linear dependency within 20 to 40 °C of the resistance measurements with an entrance current of 50 µA, 100 µA and 200 µA, which proofs a highly controlled temperature adjustment in the Envirostat 2.0 chip after its integration in the new chip peryphery shown in figure 4. The coefficient of determination was higher than 0.99 for all measurements.

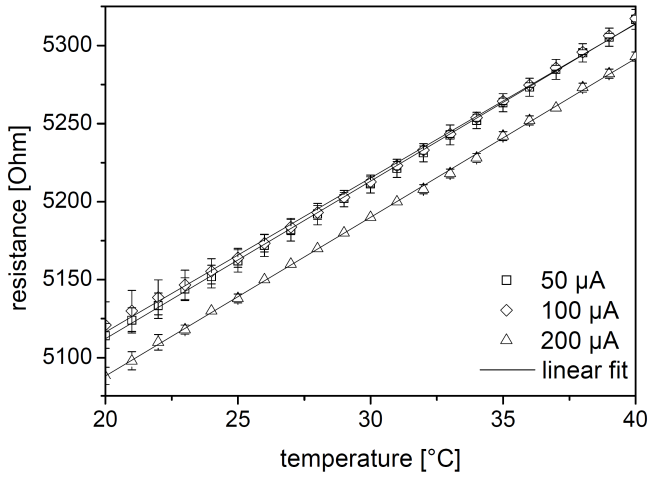

Figure 10: Electrical resistance of the on-chip microelectrode with stepwise increased temperature by the Envirostat 2.0 interface.

Calibration curves for temperature sensitive rhodamine B intensity measurements

Prior each series of rhodamine B fluorescent measurements for the characterization of Joule heating, calibration curves (i.e. fluorescence intensity vs. temperature) were determined in the cell trapping and in the point of measurement in the sorter area as described in the manuscript. Figure 11 shows exemplary the calibration curves measured in the cage center area of the two characterized 12 and 20 µm chip designs. With a coefficient of determination of at least 0.99 the decreasing intensity correlated linear with the rising temperatures.

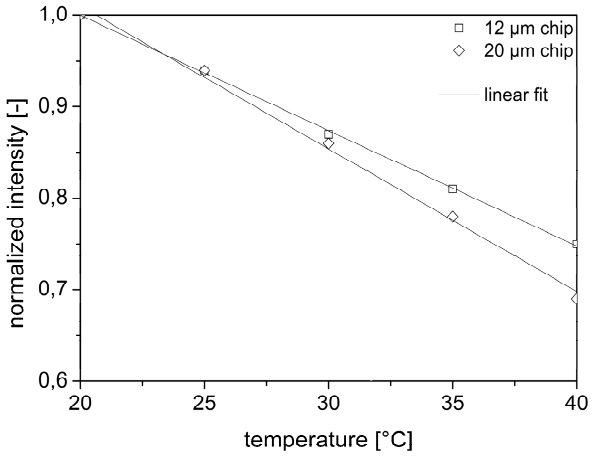

Figure 11: Normalized fluorescence intensity values of Rhodamine B allocated to the corresponding temperatures in the Envirostat 2.0. The calibration curves were obtained in the cell trapping area of cage 2 in the 12 µm and the 20 µm chip design. The solid line represents a linear fit of the experimental data. The data reflect averages of at least three independent measurements.

Example of temperature adjustment for single cell cultivation

Figure 12 shows exemplary the temperature adjustment for single cell cultivation to 30°C in the 20 µm chip design. Temperature measurements were performed using the dye Rhodamine B and fluorescence measurements as described in the manuscript in line 194. The overall temperature was set to 26.6°C and the cage activation with 2.12 V in ROT X mode resulted subsequently in a constant cultivation temperature of 30°C (Fig. 4 (A)).

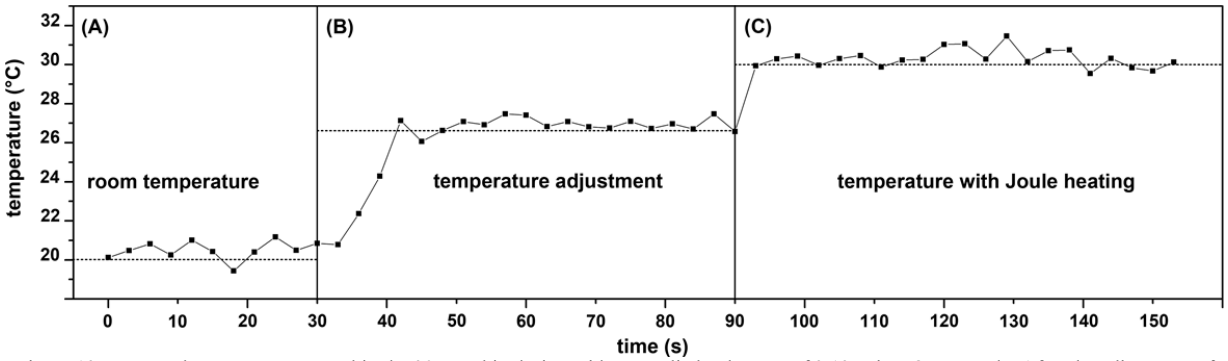

Figure 12: Temporal temperature control in the 20 µm chip design with an applied voltage$_{rms}$ of 2.12 V in ROT X mode. After the adjustment of temperature control with the Envirostat periphery and activation of the octupole cage the cultivation temperature remains stable at 30°C.

Demonstration of single bacteria isolation in the sorter section

As described in the manuscript, the zigzag electrode can be used for retention of cells which facilitates active cell sorting in the sorting (Fig 13 (A)). Adjusting the voltage allows to separate larger dividing cells from smaller single cells owing to the strong dependency of nDEP force on the cell size. In case of a to high cell concentration, it was difficult to isolate a single cell (Fig. 13 (D)). Diluting the cell concentration using the zigzag allowed reducing the number of cells in the sorting area to sort out a specific cell of interest (E), (F) and (G).

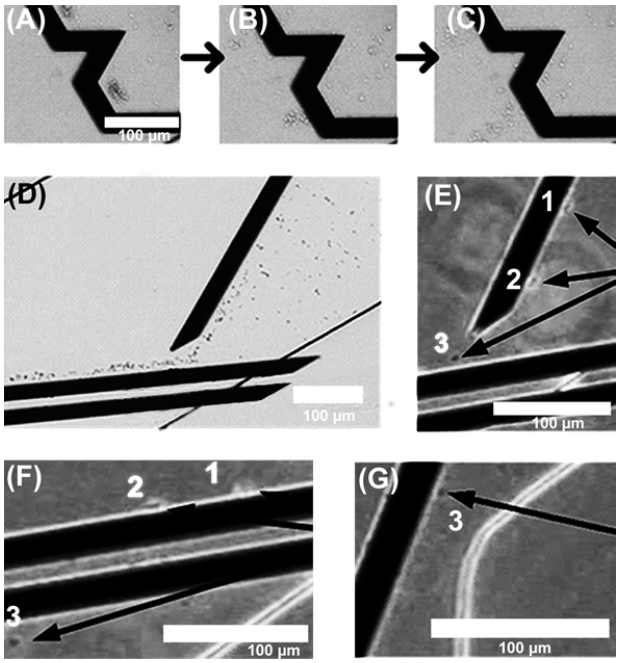

Figure 13: nDEP manipulation of *Corynebacterium glutamicum* in the sorting section of the 20 µm chip design. (A) Retention of bacteria in the zigzag electrode. (B) and (C) Release of cells in the zigzag electrode. (D) Deflection of bacteria on the deflector and gate electrode. (E) Three bacteria lined up and deflected. (F) Singularized bacterium further deflected by the fence electrode to the isolation selection.

Octupole control modes

The different force field control ACC and ROT X modes were described in detail before.[13, 25] In this work, alternating electrical fields in dipoles and octupoles were used to induce negative dielectrophoretic forces on single cells. In contrast to dipoles, octupoles allow different phase patterns, resulting in different nDEP force field configurations.[13, 25] In this work two phase patterns were used for single cell trapping, namely, the ACC mode and the ROT X mode. In the ACC mode, a two phase shifts of π was used (Fig. 14 (A))., while in the ROT X mode a four phase shift of $\pi/2$-shifted radio frequency signals are applied (Fig. 14 (B)).

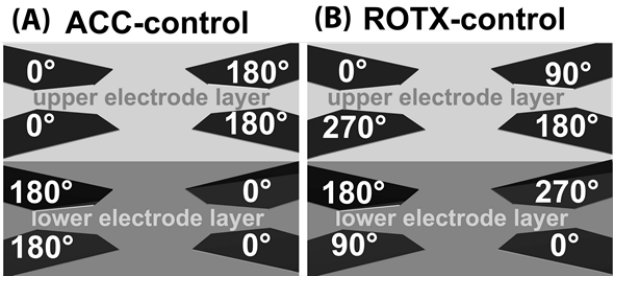

Figure 14: ACC and ROT X driving phases for cell trapping in octupoles.

nDEP cell trapping of different cell types and morphologies

Supplemental to table 2 of the manuscript, figure 15 shows exemplary the successful nDEP trapping of six different microbes. The strains differ significantly in terms of morphology and mobility. The conductivity was always adjusted to 1 S/m and the frequency was set to 6.25 MHz. The cells were trapped in the earlier described ROT X mode and in a stream velocity of approximately 10 µm/s in the octupole center. The minimal voltage used for cell trapping was dependent on changing morphology and mobility, as described in the manuscript. The analysis of minimal required voltages required to test changing applied voltages which caused temperatures varying between 24 and 34°C.

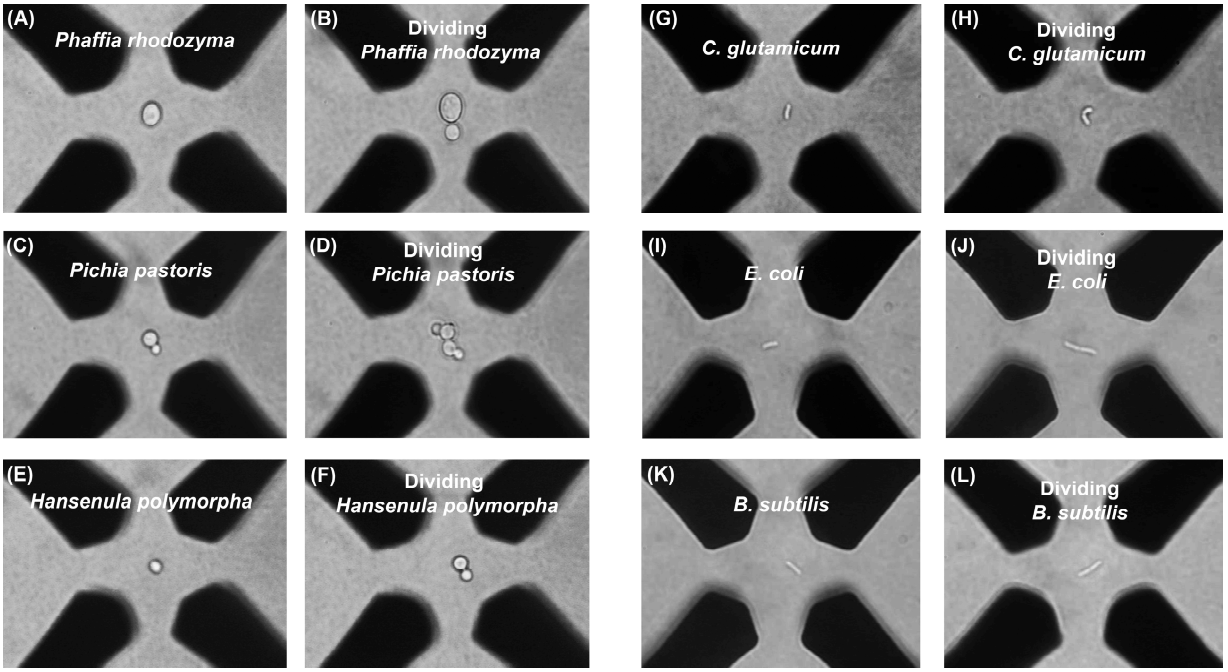

Figure 15: Single cell trapping of six different microbe strains in the 20 µm chip design.

Single bacterium growth analysis

To characterize the volumetric growth of a single bacterium in a stable temperature, the cell length was measured using the software ImageJ (Version 1.46e, Opensource, 2012) (Fig. 16).

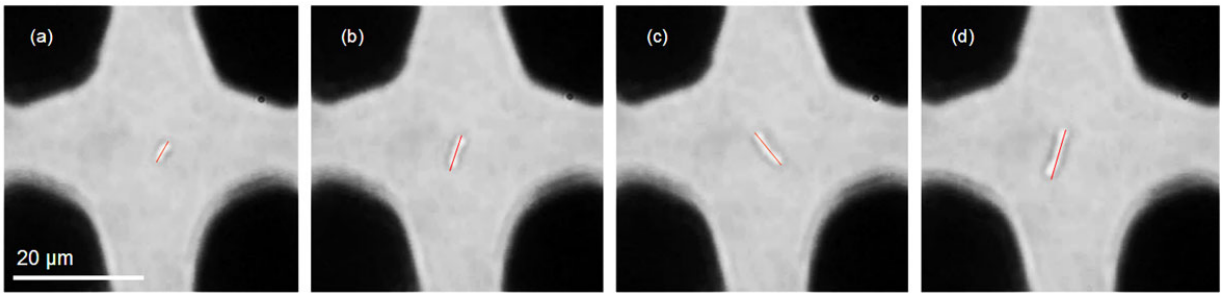

Figure 16: Example of cell size measurements for single bacterium growth characterization.

The specific growth rate was calculated with equation 10 which bases on the central assumption that cell mass linear correlates with the cell volume.

$$\frac{dV_{cell}}{dt} = \mu \times V_{cell} \quad (10)$$

where μ is the specific growth rate (h^{-1}), V_{cell} the cell volume and t the cultivation time (h). In case of *Corynebacterium glutamicum* ATCC 13032 the cell volume V_{cell} correlated well with the cell length C_l due to a stable cell diameter which allows the simple growth rate calculation as described in equation (11).

$$\frac{dC_l}{dt} = \mu \times C_l \quad (11)$$

References

1. H. A. Pohl, *J. Appl. Phys.*, 1951, **22**, 869-871.
2. T. B. Jones, *Electromechanics of Particles*, Press Syndicate of the University of Cambridge, New York, 2005.
3. T. B. Jones, *IEEE Eng. Med. Biol. Mag.*, 2003, **22**, 33-42.
4. M. Washizu and T. B. Jones, *J. Electrostat.*, 1994, **33**, 187-198.
5. H. Morgan and N. G. Green, *J. Electrostat.*, 1997, **42**, 279-293.
6. A. Sanchis, A. P. Brown, M. Sancho, G. Martinez, J. L. Sebastian, S. Munoz and J. M. Miranda, *Bioelectromagnetics*, 2007, **28**, 393-401.
7. A. Irimajiri, T. Hanai and A. Inouye, *J. Theor. Biol.*, 1979, **78**, 251-269.
8. T. Kakutani, S. Shibatani and M. Sugai, *Bioelectroch. Bioener.*, 1993, **31**, 131-145.
9. J. Voldman, *Annu. Rev. Biomed. Eng.*, 2006, **8**, 425-454.
10. R. Pethig, *Biomicrofluidics*, 2010, **4**, -.
11. T. Schnelle, T. Muller, S. Fiedler and G. Fuhr, *J. Electrostat.*, 1999, **46**, 13-28.
12. J. A. Stratton, in *(McGraw-Hill, New York)*, (Reprinted in the IEEE Press Series on Electromagnetic Wave Theory, Piscataway, NJ, 2007), 1941.
13. T. Muller, A. Pfennig, P. Klein, G. Gradl, M. Jager and T. Schnelle, *IEEE Eng. Med. Biol.*, 2003, **22**, 51-61.
14. U. Seger, M. Panayiotou, S. Schnydrig, M. Jordan and P. Renaud, *Electrophoresis*, 2005, **26**, 2239-2246.
15. C. Yang, G. Y. Tang, J. C. Chai and H. Q. Gong, *Int. J. Heat. Mass. Tran.*, 2004, **47**, 215-227.
16. T. Schnelle, R. Hagedorn, G. Fuhr, S. Fiedler and T. Muller, *Biochim. Biophys. Acta*, 1993, **1157**, 127-140.
17. G. Fuhr, H. Glasser, T. Muller and T. Schnelle, *Biochim. Biophys. Acta*, 1994, **1201**, 353-360.
18. G. Fuhr, T. Müller, T. Schnelle, R. Hagedorn, A. Voigt and S. Fiedler, *Naturwissenschaften*, 1994, **81**, 528-535.
19. G. Fuhr, T. Schnelle, R. Hagedorn and S. G. Shirley, *Cell. Eng. Inc. Mol. Eng.*, 1995, **1**, 47-57.
20. T. Müller, A. Gerardino, T. Schnelle, S. G. Shirley, F. Bordoni, G. De Gasperis, R. Leoni and G. Fuhr, *J. Phys. D: Appl. Phys.* , 1996, **29** 340–349.
21. G. Fuhr, T. Schnelle, T. Müller, H. Hitzler, S. Monajembashi and K.-O. Greulich, *Appl. Phys.*, 1998, **67**, 385–390.
22. T. Schnelle, T. Muller, G. Gradl, S. G. Shirley and G. Fuhr, *J. Electrostat.*, 1999, **47**, 121-132.
23. T. Schnelle, T. Muüller, R. Hagedorn, A. Voigt and G. Fuhr, *Biochim. Biophys. Acta*, 1999, **1428**, 99-105.
24. T. Müller, T. Schnelle, G. Gradl, S. G. Shirley and G. Fuhr, *J. Liq. Chrom. & Rel. Technol.*, 2000, **23**, 47-59.
25. T. Schnelle, T. Muller and G. Fuhr, *J. Electrostat.*, 2000, **50**, 17-29.
26. M. Dürr, J. Keutsch, T. Müller, T. Schnelle and M. Stelzle, *Electrophoresis*, 2003, **24**, 722-731.
27. M. S. Jaeger, T. Mueller and T. Schnelle, *J. Phys. D. Appl. Phys.*, 2007, **40**, 95-105.
28. M. S. Jaeger, K. Uhlig, T. Schnelle and T. Mueller, *J. Phys. D. Appl. Phys.*, 2008, **41**, 8.
29. H. Morgan, M. P. Hughes and N. G. Green, *Biophys. J.*, 1999, **77**, 516-525.
30. F. Grom, J. Kentsch, T. Muller, T. Schnelle and M. Stelzle, *Electrophoresis*, 2006, **27**, 1386-1393.
31. H. Kortmann, P. Chasanis, L. M. Blank, J. Franzke, E. Y. Kenig and A. Schmid, *Lab Chip*, 2009, **9**, 576-585.
32. J. Wu, Y. X. Ben and H. C. Chang, *Microfluid. Nanofluid.*, 2005, **1**, 161-167.
33. C. Bot and C. Prodan, *Eur. Biophys. J. Biophy.*, 2009, **38**, 1049-1059.
34. H. Kortmann, L. M. Blank and A. Schmid, *Lab Chip*, 2009, **9**, 1455-1460.

35. F. S. O. Fritzsch, H. Kortmann, J. Lonzynski, L. M. Blank and A. Schmid, *Microfluid. Nanofluid.*, 2011, **10**, 679-684.
36. T. R. Kuphaldt, in *allaboutcircuits.com*, allaboutcircuits.com, 2003, vol. I—DC.